

---

# A new two-step modeling strategy for random micro-fiber reinforced composites with consideration of primary pores

Heng Cai<sup>a</sup>, Junjie Ye<sup>a,c\*</sup>, Jinwang Shi<sup>a</sup>, Yiwei Wang<sup>a</sup>, Yang Shi<sup>a</sup>,  
Bo Huang<sup>b</sup>, Yonghe Xu<sup>c</sup>, Mohamed Saafi<sup>b</sup>, Jianqiao Ye<sup>b\*</sup>

<sup>a</sup> Shaanxi Key Laboratory of Space Extreme Detection, Key Laboratory of Ministry of Education for Electronic Equipment Structure Design, Xidian University, Xi'an 710071, China

<sup>b</sup> Department of Engineering, Lancaster University, Lancaster LA1 4YW, UK

<sup>c</sup> Yancheng Xinyongjia Petroleum Machinery Manufacturing Co., Ltd., Yancheng 224043, China

## Abstract:

This paper presents a novel procedure to evaluate mechanical properties of random micro-fiber reinforced composites with consideration of primary pores. To this end, micro-CT experiment is conducted first to detect micro-scale morphology of the constituent materials, including size of pores and arrangement of fibers, etc. On this basis, a two-step modeling strategy with consideration of primary pores is proposed. In the first step, the equivalent mechanical properties of the pore defects and the micro-fibers are determined by the 3D parametric finite volume directly averaging micromechanics (FVDAM), by which an equivalent ellipsoidal reinforcing phase composed of fibers and pores is constructed. In the second step, the equivalent pores and fibers are embedded into matrix materials to build an RVE of the composite to calculate the elastic modulus of the composite. In addition, the 3D parametric FVDAM is further extended to simulate plastic deformation of PEEK matrix under quasi-static tensile loading. The results obtained from the proposed two-step modeling strategy have a good agreement with the results from experiments.

**Keywords:** Short-fiber composites; Two-step modeling; Representative volume element (RVE); X-ray computed tomography; Porosity.

## 1. Introduction

Compared with traditional homogeneous materials, random micro fiber-reinforced composites exhibit excellent toughness, which have been widely used in both composite sheet molding and bulk molding compounds [1-4]. One of the important influencing factors in evaluating mechanical properties of composites is the existence of primary pore defects that are introduced inevitably during material processing [5-7]. Pore defects not only have a significant effect on the mechanical properties [8-9] of a composite, but also increase uncertainty of damage evolution in the composite [10-12]. Therefore, how to evaluate mechanical properties of micro fiber-reinforced composites with consideration of primary pore defects is worthy of further investigation.

Historical studies on pore defects can be divided into two main categories. The first category focused on a range of pore sizes from meso-scale (mm) to micro-scale ( $\mu\text{m}$ ) that exist synchronously in a composite. For instance, Huang et al. [13] investigated pore defects at different scales and applied periodical boundary conditions to micro-scale RVEs of fiber tows, as well as meso-scale RVEs of woven composites to determine their elastic modulus. The simulation results indicated that mechanical properties of the composites were more sensitive to the pores in fiber bundles. The second category of the studies focused on investigating mechanical properties of composites at a single geometric scale, which paid more attention to morphology and location of pore defects. With respect to pore distributed in matrix and fiber bundle, Mekonnen et al. [14] developed a finite element model, which demonstrated that elastic modulus gradually decreased

\*Corresponding authors.

Email address: ronkey6000@sina.com (Junjie Ye)  
j.ye2@lancaster.ac.uk (Jianqiao Ye)

---

when more pore defects were considered. Wei et al. [15] investigated the influence of pore defects on thermal expansion coefficient of composites, and employed a finite element method to calculate their thermal expansion coefficients. In addition, Yang et al. [16] established a Voronoi-structure model and evaluated equivalent shear modulus of composites with different pore shapes by finite element software. The numerical results were in good agreement with the results from compression tests. Cao et al. [17] proposed a fast Fourier transform to obtain equivalent elastic modulus of rock materials with pores and investigated the influence of pore orientation on the nonlinear mechanical behaviors of the materials.

To develop a reliable numerical model, accurate microstructural parameters from experimental tests are important prerequisites. Here, a brief comparison of some main test methods in determining pore defects is introduced. The density measurement method was firstly proposed to estimate pore volume. The method is easy to follow, as test standards, such as ASTM D2734 [18], ASTM D3171 [19], ASTM D2584 [20], etc., are readily available. However, the accuracy of this method is normally low [2]. Compared with the density measurement method, scanning electron microscope (SEM) can be employed to directly characterize two dimensional pore structures. The porosity statistically calculated from the scan images are limited to the selected surfaces of specimens [21]. Ultrasonic test, as a typical non-destructive test method, can measure microstructure of pores by scanning in different directions without causing damage to the specimens. It should be noted, however, that ultrasonic tests are restricted to exploring micro-scale morphology of regular pores [22]. At present, micro computed tomography (micro-CT) is the most popular experimental method to characterize 3D micro-scale morphology in composites, including pore defects, 3D fiber arrangement, etc. [23] Although it is more time consuming in obtaining scanning data, it is compensated by offering high-precision microstructural parameters [24]. Overall, CT scanning technology provides an effective experimental measure in investigating 3D morphology of pores in composites.

Previous studies, e.g., in [25], concluded that pore defects resulted in a significant reduction in stiffness of random micro-fiber reinforced composites. To effectively evaluate their mechanical properties with a high accuracy, micro-CT is firstly used in this paper to explore 3D micro-scale morphology of fiber distribution, pore ratio, etc. Furthermore, a two-step modeling scheme is proposed to predict the effective moduli and nonlinear deformation of micro-fiber reinforced composites. The outline of this paper is as follows: micro-CT test is employed to analyze distribution and volume fraction of pore defects in Section 2. In Section 3, a new two-step modeling strategy with consideration of primary pore defects is presented. Moreover, an effective elastic-plastic constitutive model is proposed to describe nonlinear deformation of composites with consideration of pore defects. A comparison between numerical results and experimental tests is shown in Section 4. The conclusions can be found in Section 5.

## 2 Micro-scale primary pore defects

### 2.1. Micro-CT system

To determine the geometric parameters of micro-scale pore structure in the micro-fiber reinforced composites using Micro-CT, a  $1\text{cm} \times 2.5\text{mm} \times 2.5\text{mm}$  specimen was prepared. Fig. 1 is the schematic diagram of the Micro-CT test, which has three stages, i.e., the scanning, the control and the image mosaic stages. From the attenuation of the X-ray emitted from a tube of circular cross-section, a series of two-dimensional micro-scale slices perpendicular to the X-ray direction are

collected. To obtain an accurate three-dimensional structural topology, multi-group scanning images are needed by rotating the object and reconstructing its 3D structure using computer. A post-processing software is required to analyze the micro-structure and extract objective CT data according to the determined threshold values of the constituent materials. Although the test specimen is relatively small, sufficient scanning time should be allowed to obtain the required microscopic parameters accurately. Herein Zeiss Xradia 510 versa is used and the scanning time of each test is nearly 12 hours. During the tests, the recorded tube voltage and power are 70keV and 10W, respectively. To capture the information with a higher accuracy, the scanning accuracy is maintained at 0.5mm/pixel during the experimental tests.

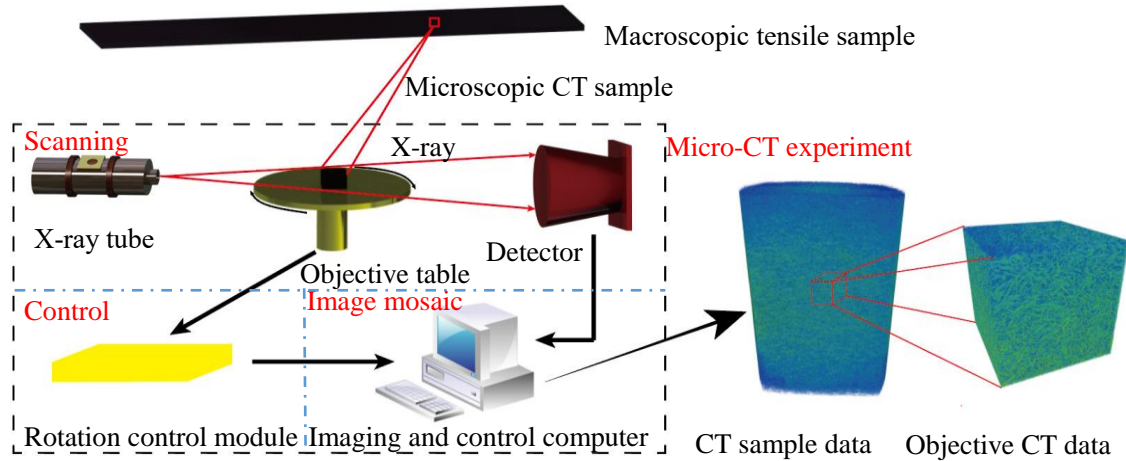


Fig. 1. Micro-CT experiment schematic diagram

## 2.2. Threshold segmentation of the constituent materials

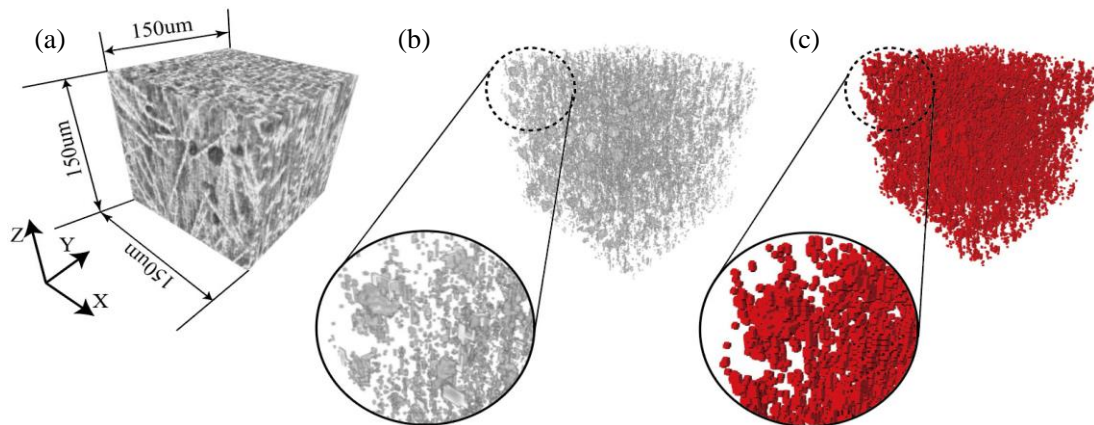


Fig. 2. Determination of the threshold value: (a) Sub-volume to be investigated (b) Original CT image with pore defects (c) The corresponding pixel image

It has been observed that the effective mechanical property of the composite with consideration of micro features (such as spatial orientation, length, pore size, sphericity, etc.) tends to be stable and independent of location when the selected RVE is sufficiently large. It is also noted that a smaller specimen provides more accurate image threshold of the constituent materials, which are distinguished according to their boundary characteristics. Experimental tests have suggested that a  $150\mu\text{m} \times 150\mu\text{m} \times 150\mu\text{m}$  (Fig. 2) sub-volume extracted from the specimen offers a satisfactory compromise between accuracy and computational efficiency. The micro-scale coordinate system in Fig. 2(a) is identical to that used in the macroscopic tensile tests, which is convenient to analyze

distribution and formation of pores. Fig. 2(b) is the segmented image using the threshold of air. It can be seen from the zoom-in image that different size of the pore defects can be detected. To evaluate the pore volume, the three-dimensional air medium is further converted into the pixel format shown in Fig. 2(c). Although the surface of the 3D pixel image is slightly less smooth, the data are more convenient for Boolean operation [26] to determine the specific geometric parameters of the constituent materials. On this basis, Avizo software is used and the thresholds are calibrated and determined in the range of 0~65535. It is worth mentioning that the threshold ranges are linked to mass density in the X-ray CT images. The respective threshold ranges of the pore defects, matrix and micro-fibers are shown in Table 1.

**Table 1.** Threshold ranges of constituent materials

| Materials       | Pores   | PEEK        | E-glass fiber |
|-----------------|---------|-------------|---------------|
| Threshold range | 0-15600 | 15600-23500 | 23500-65535   |

### 2.3. Validation of the determined threshold

The threshold value of the air medium in the CT images has been determined in Section 2.2. Herein the pore defects in a 1mm×1mm 2D plane slice extracted from the 3D CT image are calibrated as shown in Fig. 3(a). The pore defects are marked green in Fig.3(b) to highlight the primary pore defects. From a detailed comparison, it can be concluded that the pore defects in Fig. 3(a) are practically covered by those green spots in Fig. 3(b) according to the determined threshold. In other words, the pore distribution in the micro-fiber reinforced composite can be accurately determined by the calibrated thresholds derived from the CT images.

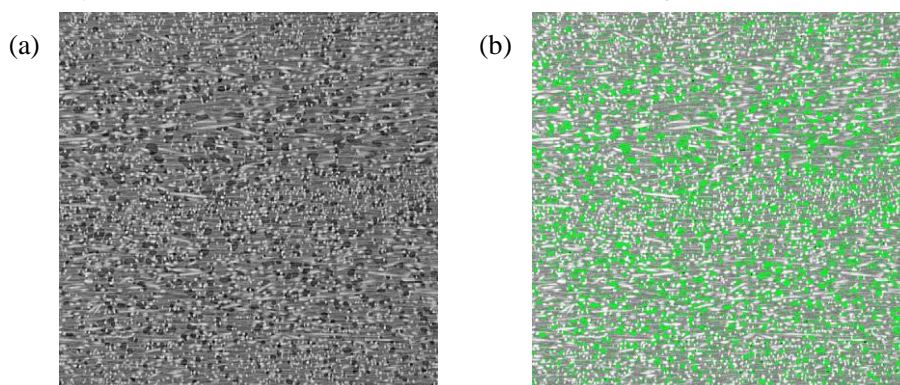


**Fig. 3.** Calibration of the threshold value: (a) Original two-dimensional CT slice (b) two-dimensional CT slice with highlighted pore defects

Using the determined thresholds, the correlation law of pore distribution can be established by investigating the selected 3D sub-image shown in Fig. 4(a). During the preparation process, the micro-fibers mixed in the resin unidirectionally flows along the  $x$ -axis into the mold and the mold compression is perpendicular to the resin flow. To study the distribution of the pores in the micro-fiber reinforced composites, three plane slice images in the  $x_1$ - $y_1$ , the  $x$ - $z$  and the  $y$ - $z$  planes are, respectively, taken and shown in Figs. 4(b)-(d). It can be found from Fig. 4(b) that most of the pore defects (in green color) are distributed around the fibers and of irregular morphology. From a comparison of Figs. 4(b)-4(d), it can be found that the pore size in the  $x_1$ - $y_1$  plane is much greater, and the distribution of the fibers is more random, resulting in more space between fibers. In other words, the size of pores and the space between fibers in the  $y$ - $z$  plane, as shown in Fig. 4(c), are relatively smaller. In addition, a few primary pores distributed in the upper and lower edges can be found in Fig. 4(c)-(d). This may be attributed to a combined action of resin flow and mold

compression.

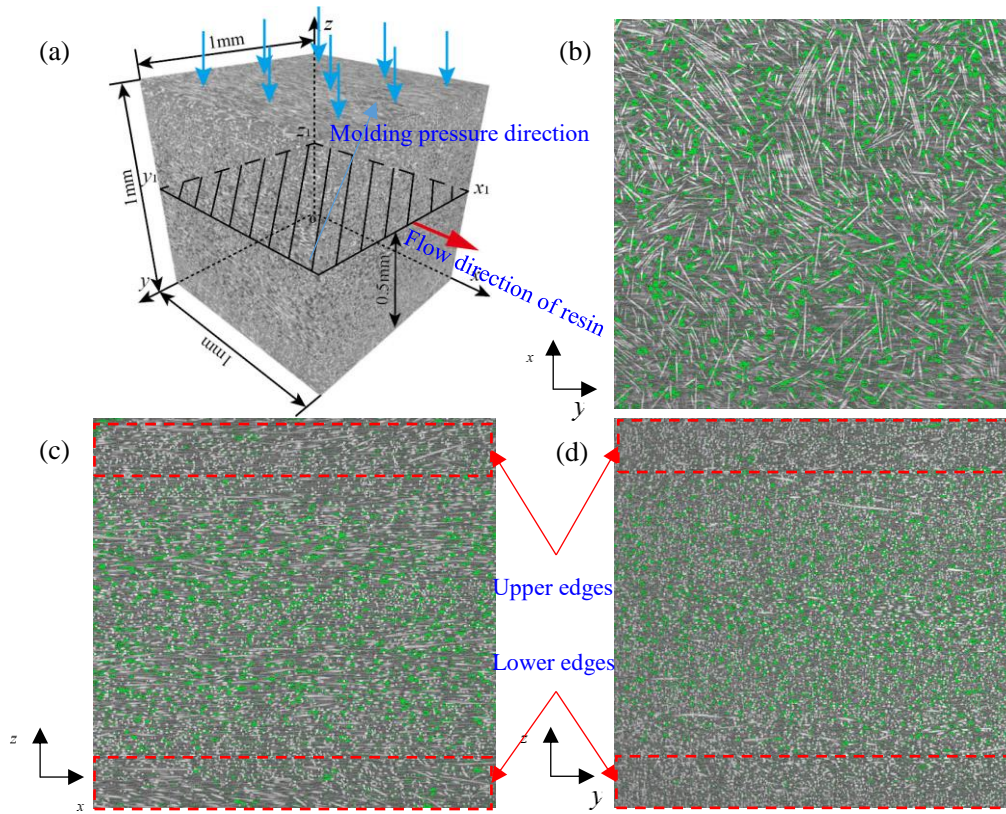


**Fig. 4.** Distribution of the pore defects: (a) three-dimensional topography of the extracted sub-volume  $1\text{mm} \times 1\text{mm} \times 1\text{mm}$  (b) two-dimensional CT slice in  $x_1\text{-}y_1$  plane (c) two-dimensional CT slice in  $x\text{-}z$  plane (d) two-dimensional CT slice in  $y\text{-}z$  plane

#### 2.4. Statistics of pore defects

Based on the preliminary research reported above, the 3D morphology of the primary pores can be obtained, as shown in Fig. 5. Herein the pore defects are tinted with different colors for easy identification. Obviously, it is impossible to implement this irregular 3D micro-scale morphology of pores in any existing numerical models.

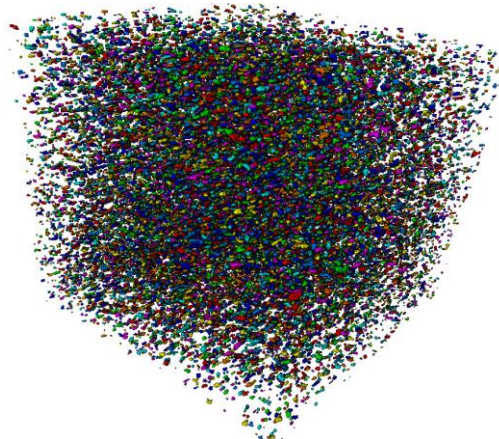


**Fig. 5.** Micro-scale geometrical morphology of pore defects extracted from the  $1\text{mm} \times 1\text{mm} \times 1\text{mm}$  sub-

Fig. 6(a) shows the statistical distribution of the pore volume, which is obtained by the post-processing software Avizo. It can be seen that the volumes of most of the pores are within the range of  $200\mu\text{m}^3$  to  $1600\mu\text{m}^3$ . From the zoom-in image, it can be seen that the largest pore is

approximately  $6400\mu\text{m}^3$ . Based on the assumption that pores in the composite can be equivalent to a pore system composed of only spherical pores, the statistical distribution of pore volume can be converted to statistical distribution of pore diameters, as shown in Fig. 6(b), by the following formula,

$$D = \sqrt[3]{\frac{6V}{\pi}} \quad (1)$$

where  $D$  and  $V$  denote diameter and volume of a pore, respectively.

Fig. 6(b) shows that the diameters of most of the pore defects are concentrated in the range of  $8\mu\text{m}$  to  $12\mu\text{m}$ , and the maximum and minimum diameters of the pores are  $23.6\mu\text{m}$  and  $6.7\mu\text{m}$ , respectively. Since the approximate length of the micro-fibers is about  $14\mu\text{m}$ , both the pore defects and the fibers can be modelled at the same scale. According to the statistical analysis, the number and the volume ratio of the pores in the  $1\text{mm} \times 1\text{mm} \times 1\text{mm}$  sub-volume are 143975 and 17.32%, respectively.

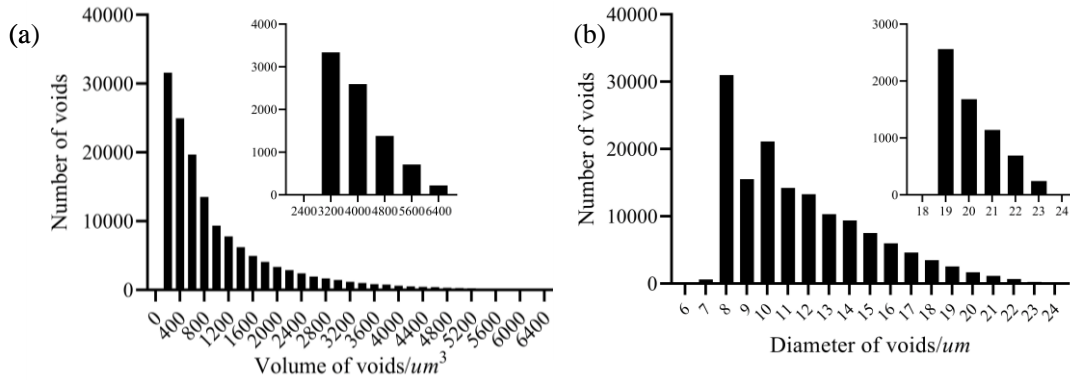


Fig. 6. Statistical analysis of pore size (a) Volume of the pore defects (b) Diameter of the pore defects

### 3 Numerical model

#### 3.1. Elastoplastic constitutive equation

The Finite Volume Direct Averaging Micromechanics (FVDAM) proposed by Pindera [27-28] is capable of studying effective modulus and stress-strain relation of continuous fiber-reinforced composites. Inspired by the high-fidelity generalized method of cells [29], the high-order terms in the 2D FVDAM are ignored to improve its computational efficiency [30]. In recent years, the FVDAM has been extended to investigate effective properties of 3D particle-reinforced or short fiber-reinforced composites, whose representative volume element is discretized by parametric meshes [31-34], where the iso-parametric FVDAM is further extended to explore nonlinear behaviors of random fiber-reinforced composites with consideration of primary pores. For a selected RVE, as shown in Fig. 7(a), it is divided first into  $N_1$ ,  $N_2$  and  $N_3$  sub-cells along the  $y_1$ -,  $y_2$ - and  $y_3$ -directions, respectively, in the local coordinate system. The sub-cell displacements  $u_i^{(\alpha\beta\gamma)}$  can be split into a combination of macroscopic displacements and microscopic fluctuate displacements  $u_i^{r(\alpha\beta\gamma)}$ , that is,

$$u_i^{(\alpha\beta\gamma)}(x, y(\zeta, \eta, \xi)) = \bar{\varepsilon}_{ij} x_j + u_i^{r(\alpha\beta\gamma)}(\zeta, \eta, \xi) \quad (2)$$

$$y_i^{(\alpha\beta\gamma)}(\zeta, \eta, \xi) = \sum_{p=1}^8 N_p(\zeta, \eta, \xi) y_i^{p(\alpha\beta\gamma)}, i = 1, 2, 3 \quad (3)$$

where  $x$  and  $y$  represent macroscopic and microscopic coordinates, respectively. The superscripts  $\alpha$ ,  $\beta$  and  $\gamma$  are sub-cell numbers. The symbols,  $p$  and  $i$ , indicate sub-cell vertices and

micro-scale coordinate directions in the local coordinate system, respectively. Here, it is worth mentioning that the parametric coordinates,  $\zeta$ ,  $\eta$  and  $\xi$ , in the local coordinate system are always between -1 and 1. The sub-cell vertex coordinates are linearly interpolated by employing shape functions,  $N$ , to establish the relationship between the sub-cell vertices in the coordinate system  $y_1$ - $y_2$ - $y_3$  (Fig. 7(b)) and the parametric coordinate system  $\zeta$ - $\eta$ - $\xi$  (Fig. 7(c)). The mapping between the two co-ordinate systems is determined by the Jacobian matrix  $J$ . The expressions of the shape function, the Jacobian matrix and the homogenized Jacobian matrix  $\bar{J}$  are shown in Refs. [31-32].  $n_i^{p(\alpha\beta\gamma)}$  are directional cosines that are the cosines of the angle between the sub-cells surfaces and the planes  $y_1$ - $y_2$ ,  $y_1$ - $y_3$  and  $y_2$ - $y_3$ , respectively.

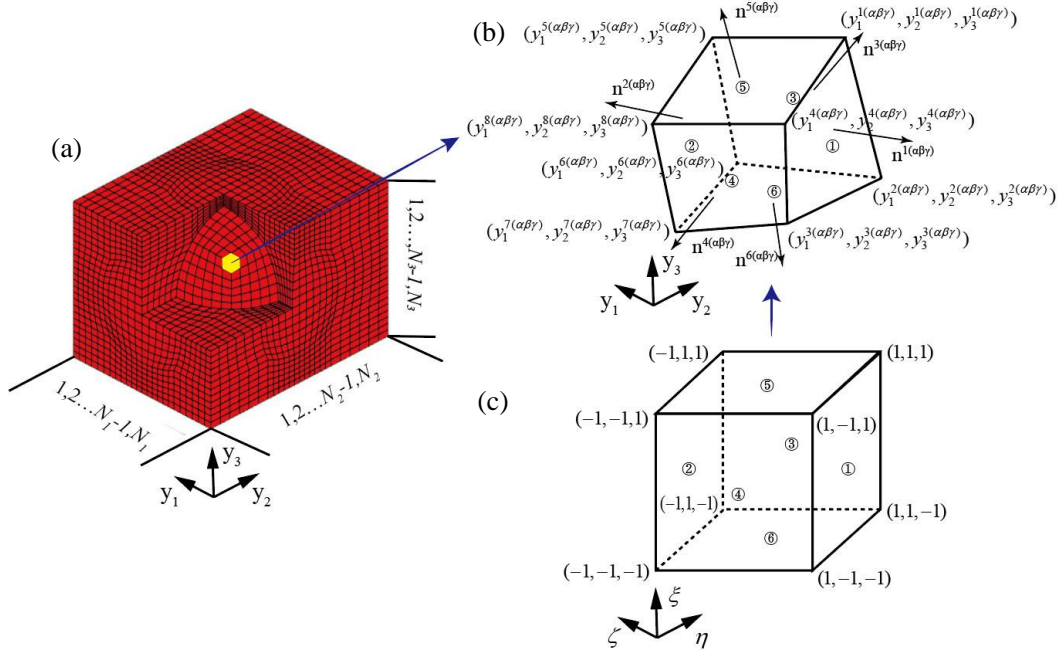


**Fig. 7.** Schematic diagram of parametric transformation of the sub-cell : (a) 3-dimensional representative volume element (b) Iso-parametric element (c) Regular hexahedral element

Quadratic expansion of Legendre polynomials is used to express the microscopic displacement in the parametric coordinates, as follows,

$$u_i^{r(\alpha\beta\gamma)}(\zeta, \eta, \xi) = W_{i(000)}^{(\alpha\beta\gamma)} + \zeta W_{i(100)}^{(\alpha\beta\gamma)} + \eta W_{i(010)}^{(\alpha\beta\gamma)} + \xi W_{i(001)}^{(\alpha\beta\gamma)} + \frac{1}{2}(3\zeta^2 - 1)W_{i(200)}^{(\alpha\beta\gamma)} + \frac{1}{2}(3\eta^2 - 1)W_{i(020)}^{(\alpha\beta\gamma)} + \frac{1}{2}(3\xi^2 - 1)W_{i(002)}^{(\alpha\beta\gamma)} \quad (4)$$

where,  $W_i^{(\alpha\beta\gamma)}$  are the micro-variables in the local coordinate system. By homogenizing the micro-scale displacements in the  $\zeta$ - $\eta$ - $\xi$  coordinate system, the linear relationship between the surface-averaged displacements of an iso-parametric sub-cell and the micro-variables can be obtained,

$$\bar{u}_i^{r(1,2)} = \frac{1}{4} \int_{-1}^1 \int_{-1}^1 u'(\mp 1, \eta, \xi) d\eta d\xi = W_{i(000)} \mp W_{i(100)} + W_{i(200)} \quad (5)$$

$$\bar{u}_i^{r(3,4)} = \frac{1}{4} \int_{-1}^1 \int_{-1}^1 u'(\zeta, \mp 1, \xi) d\zeta d\xi = W_{i(000)} \mp W_{i(010)} + W_{i(020)} \quad (6)$$

$$\bar{u}_i^{r(5,6)} = \frac{1}{4} \int_{-1}^1 \int_{-1}^1 u'(\zeta, \eta, \mp 1) d\zeta d\eta = W_{i(000)} \mp W_{i(001)} + W_{i(002)} \quad (7)$$

where superscripts 1,2,...,6 are sub-cell surface numbers, as shown in Fig. 7(c). According to Eqs. (5)- (7), the first- and second-order micro-variables can be determined by the surface-averaged

displacements and the zero-order micro-variables, the detailed expressions of which can be found in Refs. [31-32]. Based on the strain-displacement relations, the sub-cell strains can be calculated by Eq. (8).

$$\varepsilon_{ij}(x, y) = \bar{\varepsilon}_{ij} + \frac{1}{2} \left( \frac{\partial u'_i}{\partial y_j} + \frac{\partial u'_j}{\partial y_i} \right) = \bar{\varepsilon}_{ij} + \varepsilon'_{ij}(\zeta, \eta, \xi) \quad (8)$$

Similarly, the sub-cell strains can be divided into macroscopic and microscopic strains. The expressions of the microscopic strain in terms of the Jacobian matrix are presented in Appendix A.1.

According to the Cauchy's stress theorem, the surface tractions can be determined by the sub-cell stresses as follows

$$t_j^{p(\alpha\beta\gamma)} = \sigma_{ij}^{(\alpha\beta\gamma)} n_i^{p(\alpha\beta\gamma)} \quad (i, j = 1, 2, 3; p = 1, 2, \dots, 6) \quad (9)$$

where

$$\sigma_{ij}^{(\alpha\beta\gamma)} = C_{ijkl}^{(\alpha\beta\gamma)} : (\varepsilon_{kl}^{(\alpha\beta\gamma)} - \varepsilon_{kl}^{in(\alpha\beta\gamma)}) \quad (10)$$

is the constitutive equation of the constituent materials. In Eqs. (9)-(10),  $\varepsilon_{kl}^{in(\alpha\beta\gamma)}$  and  $t_i^{p(\alpha\beta\gamma)}$  denote sub-cell inelastic strains and surface tractions, respectively. The expressions of Eqs. (9)-(10) can be found in Appendix A.2-A.3.

By introducing Appendix A.1-A.3 into Eq. (9), and averaging the sub-cell surface tractions, the average surface tractions can be obtained as,

$$\bar{t}_i^{(1,2)} = \frac{1}{4} \int_{-1}^1 \int_{-1}^1 t_i^{(1,2)}(\mp 1, \eta, \xi) d\eta d\xi \quad (11)$$

$$\bar{t}_i^{(3,4)} = \frac{1}{4} \int_{-1}^1 \int_{-1}^1 t_i^{(3,4)}(\zeta, \mp 1, \xi) d\zeta d\xi \quad (12)$$

$$\bar{t}_i^{(5,6)} = \frac{1}{4} \int_{-1}^1 \int_{-1}^1 t_i^{(5,6)}(\zeta, \eta, \mp 1) d\zeta d\eta \quad (13)$$

By solving Eqs. (11)-(13), the three unknown zero-order sub-cell micro-variables can be obtained. According to the Gauss Divergence Theorem [27], the sum of the average surface tractions of a sub-cell is zero, that is,

$$\int_V \nabla \cdot \sigma dV = \int_S \sigma \cdot n dS = \int_S \bar{t}_i^{(\alpha\beta\gamma)} dS^{(\alpha\beta\gamma)} = \sum_{p=1}^6 S_p^{(\alpha\beta\gamma)} \bar{t}_i^{p(\alpha\beta\gamma)} = 0 \quad (14)$$

where the detailed solutions can be found in Appendix A.4. Substituting Appendix A.1-A.3 into Eq. (14), the three unknown zero-order micro-variables can be determined as,

$$\begin{bmatrix} W_{1(000)} \\ W_{2(000)} \\ W_{3(000)} \end{bmatrix}^{(\alpha\beta\gamma)} = \Phi^{-1} \Theta \begin{bmatrix} \bar{u}'_1^{(1)} & \bar{u}'_2^{(1)} & \bar{u}'_3^{(1)} & \bar{u}'_1^{(3)} & \bar{u}'_1^{(4)} & \bar{u}'_3^{(3)} & \bar{u}'_1^{(5)} & \bar{u}'_2^{(5)} & \bar{u}'_3^{(5)} \\ + & + & + & + & + & + & + & + & + \\ \bar{u}'_1^{(2)} & \bar{u}'_2^{(2)} & \bar{u}'_3^{(2)} & \bar{u}'_1^{(4)} & \bar{u}'_2^{(4)} & \bar{u}'_3^{(4)} & \bar{u}'_1^{(6)} & \bar{u}'_2^{(6)} & \bar{u}'_3^{(6)} \end{bmatrix}^{T(\alpha\beta\gamma)} \quad (15)$$

where the expressions of  $\Phi$  and  $\Theta$  can be found in Ref. [32]. According to Eqs. (5)-(14), the relationship between the displacements and the average surface tractions of each sub-cell can be determined. In addition, by employing Eq. (15) and Appendix A.1-A.3, the 21 sub-cell micro-variables can be solved. Furthermore, the sub-cell average surface tractions can be expressed by the micro-variables, that is,

$$\bar{\mathbf{t}} = \mathbf{NC}(\bar{\boldsymbol{\varepsilon}} - \boldsymbol{\varepsilon}^{in}) + \bar{\mathbf{A}}\mathbf{W} \quad (16)$$

By substituting Eq. (14) and Appendix A.1-A.3 into Eq. (16), the relationship between the displacements and the average surface tractions of each sub-cell can be expressed as,

$$\bar{\mathbf{t}} = \mathbf{NC}(\bar{\boldsymbol{\varepsilon}} - \boldsymbol{\varepsilon}^{\text{in}}) + \bar{\mathbf{A}}\bar{\mathbf{B}}\mathbf{u} \quad (17)$$

or

$$\bar{\mathbf{t}} = \bar{\mathbf{K}}\mathbf{u} + \mathbf{NC}(\bar{\boldsymbol{\varepsilon}} - \boldsymbol{\varepsilon}^{\text{in}}) \quad (18)$$

where the product of matrices  $\bar{\mathbf{A}}$  and  $\bar{\mathbf{B}}$  is replaced by  $\bar{\mathbf{K}}$ . The details of matrices  $\bar{\mathbf{A}}$ ,  $\bar{\mathbf{B}}$ ,  $\mathbf{N}$  and  $\mathbf{C}$  are shown in [Appendix A.5-A.10](#). In addition, all of the sub-cell local stiffness matrices can be found in [Appendix A.11](#). To compute the global stiffness matrix, the following continuous and periodic conditions of displacements and average surface tractions between adjacent sub-cells are imposed, as shown in [Fig. 8](#),

$$\begin{aligned} \bar{\mathbf{u}}_i^{r1(\alpha\beta\gamma)} &= \bar{\mathbf{u}}_i^{r2(\alpha+1,\beta,\gamma)} = \hat{\mathbf{u}}_i^{r1(\alpha+1,\beta,\gamma)} & \bar{\mathbf{u}}_i^{r1(N_\alpha\beta\gamma)} &= \bar{\mathbf{u}}_i^{r2(1\beta\gamma)} = \hat{\mathbf{u}}_i^{r1(1\beta\gamma)} \\ \bar{\mathbf{u}}_i^{r3(\alpha\beta\gamma)} &= \bar{\mathbf{u}}_i^{r4(\alpha,\beta+1,\gamma)} = \hat{\mathbf{u}}_i^{r2(\alpha,\beta+1,\gamma)} & \bar{\mathbf{u}}_i^{r1(N_\alpha\beta\gamma)} &= \bar{\mathbf{u}}_i^{r2(1\beta\gamma)} = \hat{\mathbf{u}}_i^{r1(1\beta\gamma)} \end{aligned} \quad (19)$$

$$\begin{aligned} \bar{\mathbf{u}}_i^{r5(\alpha\beta\gamma)} &= \bar{\mathbf{u}}_i^{r6(\alpha,\beta,\gamma+1)} = \hat{\mathbf{u}}_i^{r3(\alpha,\beta,\gamma+1)} & \bar{\mathbf{u}}_i^{r1(N_\alpha\beta\gamma)} &= \bar{\mathbf{u}}_i^{r2(1\beta\gamma)} = \hat{\mathbf{u}}_i^{r1(1\beta\gamma)} \\ \bar{\mathbf{t}}_i^{r1(\alpha\beta\gamma)} + \bar{\mathbf{t}}_i^{r2(\alpha+1,\beta,\gamma)} &= 0 & \bar{\mathbf{t}}_i^{r1(N_\alpha\beta\gamma)} + \bar{\mathbf{t}}_i^{r2(1\beta\gamma)} &= 0 \\ \bar{\mathbf{t}}_i^{r3(\alpha\beta\gamma)} + \bar{\mathbf{t}}_i^{r4(\alpha,\beta+1,\gamma)} &= 0 & \bar{\mathbf{t}}_i^{r3(\alpha N_\beta\gamma)} + \bar{\mathbf{t}}_i^{r4(\alpha 1\gamma)} &= 0 \\ \bar{\mathbf{t}}_i^{r5(\alpha\beta\gamma)} + \bar{\mathbf{t}}_i^{r6(\alpha,\beta,\gamma+1)} &= 0 & \bar{\mathbf{t}}_i^{r5(\alpha\beta N_\gamma)} + \bar{\mathbf{t}}_i^{r6(\alpha\beta 1)} &= 0 \end{aligned} \quad (20)$$

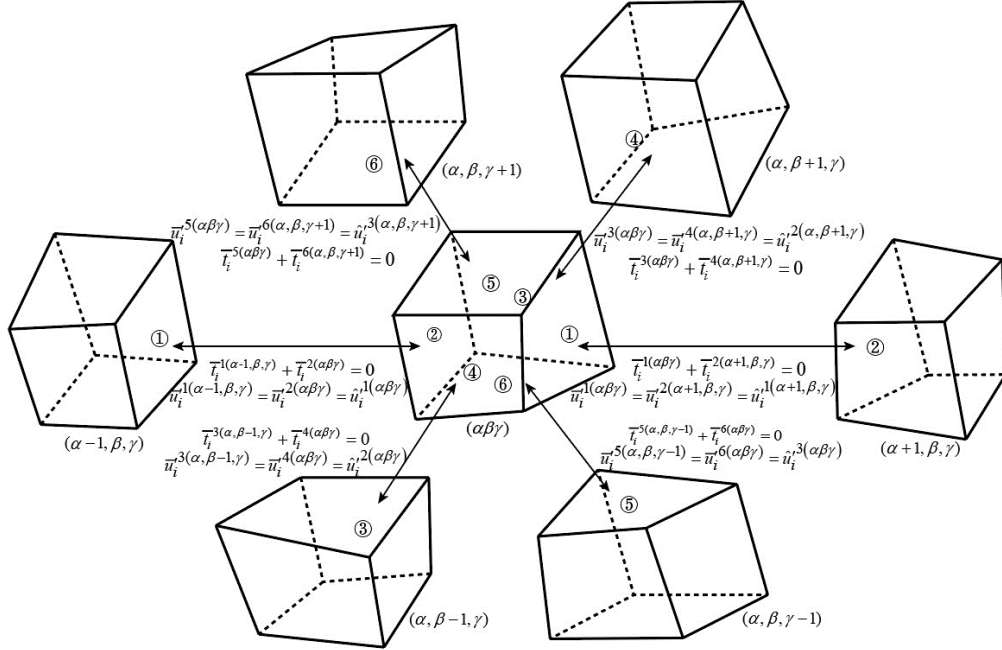


Fig. 8. Continuous condition between the adjacent sub-cells

The global stiffness equation can be obtained by introducing [Eqs. \(19\)-\(20\)](#) into [Eq. \(18\)](#), that is,

$$\bar{\mathbf{K}}\bar{\mathbf{u}} = \Delta\mathbf{C}\bar{\boldsymbol{\varepsilon}} - \Delta\mathbf{C}_1\bar{\boldsymbol{\varepsilon}}^{\text{in}1} - \Delta\mathbf{C}_2\bar{\boldsymbol{\varepsilon}}^{\text{in}2} \quad (21)$$

which is subjected to the continuous and periodic conditions in [Eqs. \(19\)-\(20\)](#). Further details of [Eq. \(21\)](#) are shown in [Appendix B.1-B.9](#). The expressions of matrices  $\bar{\mathbf{K}}$ ,  $\Delta\mathbf{C}$ ,  $\Delta\mathbf{C}_1$  and  $\Delta\mathbf{C}_2$  are shown in [Appendix B.10](#).

### 3.2. A two-step modeling strategy

In reference [25], the authors focused on developing a simple model that can consider random short fibers and testing the model against effective moduli without considering initial pores, as significant experimental work on pore characteristics were required to assess the possibility of including them in the model. Also, it is essential to find a way to incorporate pores into the model without significantly increase the complexity of the modelling process. From the geometric

characteristic and microscopic properties of pore defects, micro-fibers and matrix determined by the Micro-CT images reported in the current work, a novel two-step modeling strategy with consideration of pore defects is proposed in this Section, as illustrated in Fig. 9 and summarized below.

### 3.2.1. First step- Equivalence of pores and random micro-fibers

The 3D iso-parametric FVDAM is employed to construct the micro-scale model capable of considering pore defects and random micro-fibers. Firstly, the distribution of the micro-fibers, as well as the geometric parameters of the pore defects are both defined from the CT images. It should be noted that the detailed topological structure of the individual pores cannot be considered in the numerical modeling due to the number of pore defects, which is prohibitively computational expensive. To simplify this problem, the primary pores derived from the preparation process are considered as an isotropic constituent material [35]. For the random fibers, they are equivalently represented by the isotropic yellow ellipsoid shown in Fig. 9. It should be noted that the geometrical parameters of the simple ellipsoidal model, including its principal axis direction and volume fraction are determined by the test results derived from the CT images. More details can be found from the authors' previous study [25]. For the pore defects, the equivalent cubic element in blue, is determined according to the volume fraction of the pores. The integration of the isotropic cubic pore phase with the isotropic 3D elliptical fiber phase results in an orthotropic phase represented by the purple sphere. The volume fraction of the orthotropic sphere is equal to the total volume fraction of the pores and fibers. The three-dimensional parametric FVDAM is used to establish the micro-scale model according to the micromechanical formula of composites [15]. The stress-strain relationship of the equivalent model and the equivalent stiffness  $\mathbf{C}_1$  can be calculated as follows:

$$\bar{\boldsymbol{\sigma}} = \frac{1}{V_1} \int_{V_1=V_p+V_f} \boldsymbol{\sigma}^{(\alpha\beta\gamma)} dV = \sum_{n=1}^N (v_p^{(\alpha\beta\gamma)} \boldsymbol{\sigma}_p^{(\alpha\beta\gamma)} + v_f^{(\alpha\beta\gamma)} \boldsymbol{\sigma}_f^{(\alpha\beta\gamma)}) = \mathbf{C}_1 \bar{\boldsymbol{\varepsilon}} \quad (22)$$

$$\mathbf{C}_1 = \sum_{n=1}^N (v_p^{(\alpha\beta\gamma)} \mathbf{C}_p^{(\alpha\beta\gamma)} \mathbf{A}_p^{(\alpha\beta\gamma)} + v_f^{(\alpha\beta\gamma)} \mathbf{C}_f^{(\alpha\beta\gamma)} \mathbf{A}_f^{(\alpha\beta\gamma)}) \quad (23)$$

where the subscripts,  $p$  and  $f$ , denote pores and matrix, respectively. The calculated equivalent stiffness  $\mathbf{C}_1$  is determined by the sub-cell volume  $v$ ,  $\mathbf{C}$  and  $\mathbf{A}$ , the expressions of which can be found in [31]. In fact, the orthotropic mechanical properties of  $\mathbf{C}_1$  are mainly attributed to the micro-fibers, while the existence of pores result in reduced stiffness and strength. The calculated orthotropic mechanical parameters of the RVE are to be used in the following section.

### 3.2.2. Second step- Equivalent procedure of the matrix and inclusion phase

The 3D iso-parametric FVDAM is further employed to determine the mechanical properties of the composites composed of the matrix and the equivalent fiber and pore volume obtained at the end of step 1. In detail, the equivalent orthotropic spherical phase, resulting from the integration of the pores and the micro-fibers in step 1, is introduced as the reinforcement to the matrix in the second step. The 3D parametric FVDAM algorithm is again used to establish the secondary equivalent microscale model, which integrates the purple spherical phase with the red matrix materials, as shown in Fig. 9. The average stress  $\bar{\boldsymbol{\sigma}}$  of the equivalent model in yellow can be computed as,

$$\bar{\boldsymbol{\sigma}} = \frac{1}{V_2} \int_{V_2=V_1+V_m} \boldsymbol{\sigma}^{(\alpha\beta\gamma)} dV = \sum_{n=1}^N (v_1^{(\alpha\beta\gamma)} \boldsymbol{\sigma}_1^{(\alpha\beta\gamma)} + v_m^{(\alpha\beta\gamma)} \boldsymbol{\sigma}_m^{(\alpha\beta\gamma)}) = \mathbf{C}_2 \bar{\boldsymbol{\varepsilon}} \quad (24)$$

where

$$\mathbf{C}_2 = \sum_{n=1}^N (v_1^{(\alpha\beta\gamma)} \mathbf{C}_1^{(\alpha\beta\gamma)} \mathbf{A}_1^{(\alpha\beta\gamma)} + v_m^{(\alpha\beta\gamma)} \mathbf{C}_m^{(\alpha\beta\gamma)} \mathbf{A}_m^{(\alpha\beta\gamma)}) \quad (25)$$

where the subscripts, 1 and  $m$ , represent equivalent model in the first step and of the matrix, respectively. The components,  $v_1$ ,  $\mathbf{C}_1$  and  $\mathbf{A}_1$ , represent volume fraction, stiffness matrix and Hill's matrix [36] of the equivalent model, respectively. The subscript  $m$  denotes matrix. Correspondingly,  $v_m$ ,  $\mathbf{C}_m$  and  $\mathbf{A}_m$  represent volume fraction, stiffness matrix and Hill's matrix of the matrix materials, respectively. The symbol,  $\mathbf{C}_2$ , denotes the equivalent stiffness matrix of the micro-fiber reinforced composites with primary pores.

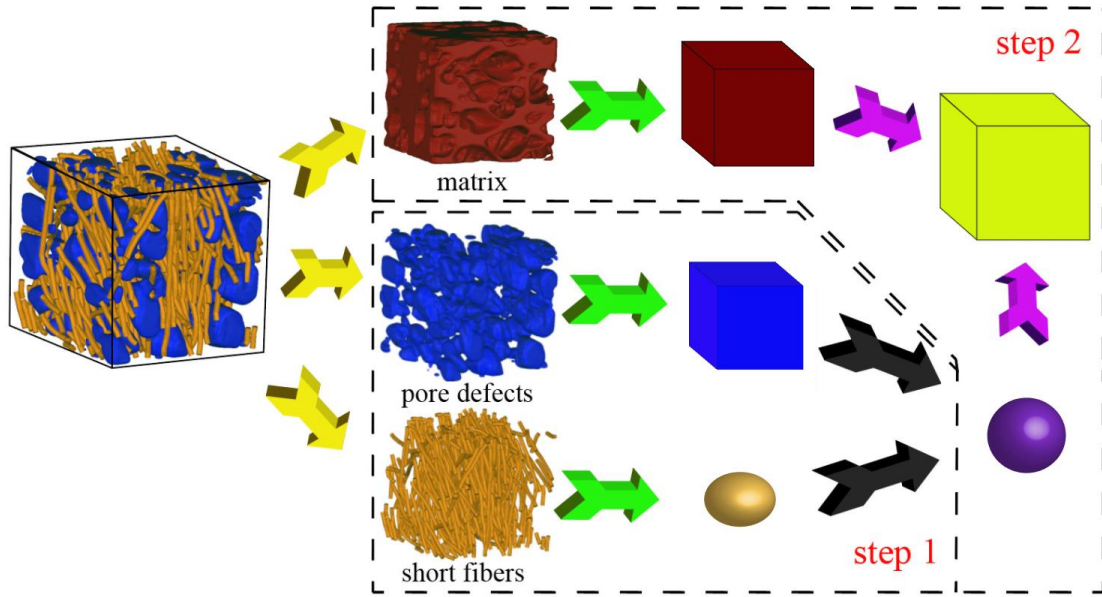


Fig. 9. Schematic diagram of the proposed two-step modeling strategy

## 4 Experimental verification

### 4.1. Shape randomness of pore defects

Shape irregularity of pore defects is an important factor in an anisotropic model [37]. Based on the spherical assumption, the spherical degree of an irregular pore is evaluated by the following equation in terms of the ratio between the actual volume and surface area of the pore,

$$R = \frac{\pi^{1/3} (6 * V_{void})^{2/3}}{A_{void}} \quad (26)$$

where  $R$  is the spherical degree of a pore defect.  $V_{void}$  and  $A_{void}$  are, respectively, the volume and the surface area of the irregular pore.

The volumes of the pores from the experiment tests have been shown in Fig. 6. Fig. 10 shows the distribution of surface area of the primary pores, whose minimum and maximum values are  $135.268\mu\text{m}^2$  and  $5472.58\mu\text{m}^2$ , respectively. Most of the surface areas are within the range of  $135\mu\text{m}^2$  and  $1400\mu\text{m}^2$ . It is interesting to mention that nearly half of the surface areas are concentrated in the range of  $200\mu\text{m}^2 \sim 600\mu\text{m}^2$ . Form the zoom-in image in Fig.10, the number of pores decreases sharply with the increase of surface area. In addition, the pores having a surface area over  $1800\mu\text{m}^2$  are less than 1%.

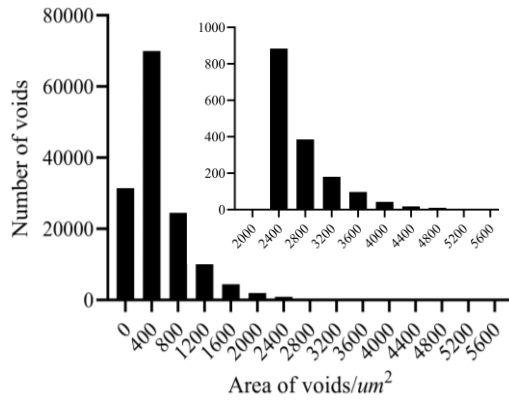


**Fig. 10.** The statistical results of pore area

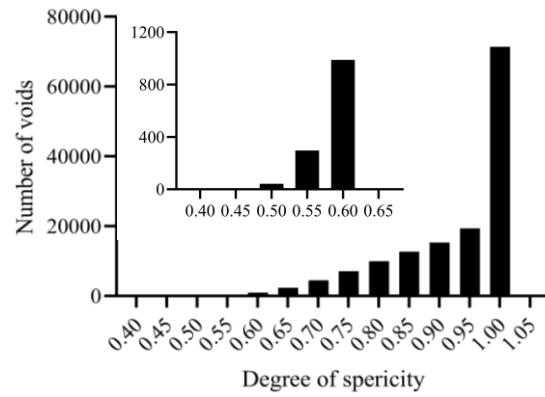


**Fig. 11.** Spherical degree of the pores

According to the spherical assumption, the spherical degree can be determined by Eq. (26). It is worth noting that the equivalent sphere presents a certain directivity once the spherical degree is less than 1. From the statistical results shown in Fig. 11, the pore defects account for 75% when the spherical degree is greater than 0.9. This proportion increases to 90% when the spherical degree is over 0.8. In addition, there is only very small amount of pore defects with a spherical degree in the range of 1~1.02. Therefore, the shape of the primary pores has little effect on the anisotropy of the micro-fiber reinforced composites. In other words, most of the primary pores are approximately spherical. Based on the above analyses, it is concluded that the pores can be assumed to be isotropic in numerical modeling.

#### 4.2. A two-step validation

To verify the proposed two-step modeling scheme, local stress distribution is calculated in the first step by the FVDAM. The influence of the number of the sub-cells on the elastic modulus of the composite is studied first and shown in Table 2. It can be seen from the table that a RVE consisting of  $24 \times 24 \times 24$  sub-cells is suffice to achieve a converged result. Thus, this meshing density is used below to calculate the elastic modulus of the composite with or without considering the effect of pores. The numerical predictions are compared with the experiment results from [25]. For the two-step modelling, the material parameters of the PEEK resin and the micro glass fibers are shown in Table 3. In the Step 1 shown in Fig.9, to construct the equivalent orthotropic hybrid inclusion of pores and fibers for the Step 2 homogenization with the matrix, the total volume of the pores must be considered and meshed in the FVDAM model, where the elastic modulus of the pores is assumed to be 0.01 times of that of the resin matrix to facilitate the numerical calculations [38] without sacrificing accuracy. This is because using zero for the modulus of pores may result in an ill-conditioned global stiffness matrix (Eq. (21)) during the numerical analysis by the FVDAM.

**Table 2.** Mesh density analysis on elastic modulus of  $0^\circ$  off-axis angle

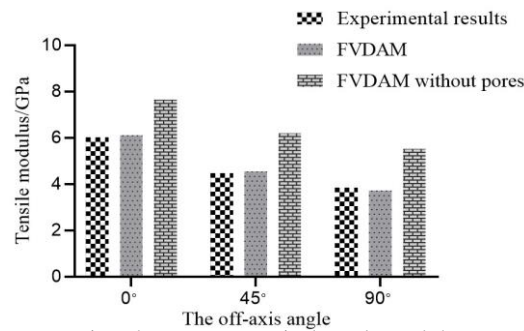
| Number of meshes    | $8 \times 8 \times 8$ | $16 \times 16 \times 16$ | $24 \times 24 \times 24$ | $28 \times 28 \times 28$ |
|---------------------|-----------------------|--------------------------|--------------------------|--------------------------|
| Elastic modulus/GPa | 4.128                 | 5.375                    | 6.049                    | 6.051                    |

Table 3 presents the properties of the constituent materials used in the numerical calculations, where the volume fractions of each constituent are obtained from CT scans. Fig. 12 shows a comparison of the elastic modulus between the numerical results and the experimental data. The results show that pore defects have significant impact on the effective modulus, and the proposed two-step method improves the accuracy of the predictions by nearly 20% when compared with using

the model without considering pore defects [25]. In detail, the maximum relative errors are equal to 1.72% and 1.12% when the off-axis angles are  $45^\circ$  and  $0^\circ$ , respectively. The calculation error of the proposed two-step method may be attributed to the ignorance of pore direction during the first-step modeling.

**Table 3.** Parameters of constituent materials at  $23^\circ\text{C}$

| Materials                    | E-glass fiber | PEEK   | Porous |
|------------------------------|---------------|--------|--------|
| Elastic modulus/GPa          | 72.4          | 3.6    | 0.036  |
| Poisson's ratio              | 0.20          | 0.39   | 0.0039 |
| Density/(g/cm <sup>3</sup> ) | 2.60          | 1.32   | -      |
| Volume fraction              | 14.41%        | 68.43% | 17.16% |



**Fig. 12.** The comparison between numerical results and the experimental data

#### 4.3. Nonlinear mechanical behaviors

To take into account the properties of all the individual constituent materials, the micro-fibers and the matrix materials are, respectively, assumed to be linear elastic and elastoplastic in the numerical simulation. To describe the nonlinear deformations in the PEEK matrix, the modified Bodner-Partom constitutive model [39-40] is employed. In this paper, the stress-strain behaviors of the composites with  $0^\circ$ ,  $45^\circ$  and  $90^\circ$  off-axis angles are obtained, respectively, and shown in Fig. 13. In detail, the curves labelled with circles and triangles are the results from numerical simulations with pores and the experimental results from [25], respectively. In general, the numerical predictions agree well with the test results. Similarly, the maximum error between the numerical and test results occurs when  $45^\circ$  off-axis load is considered. This is understandable due to the fact that in the  $0^\circ$  or  $90^\circ$  direction, which is the respective principal axis of the equivalent ellipsoid of fibers in Fig. 9, the profiles of pores and fibers are directly from the CT measurements. In the  $45^\circ$  direction, however, the profiles of pores and fibers are determined numerically from the elliptical assumption, which inevitably introduces additional errors. Nevertheless, it is evident that the comparisons have shown good agreement between the numerical and the test results in all three directions. In Figs. 13(a)-(c), the FVDAM results without considering pores are also presented for comparisons. Obviously the existence of pores reduces the stiffness of the composites significantly.

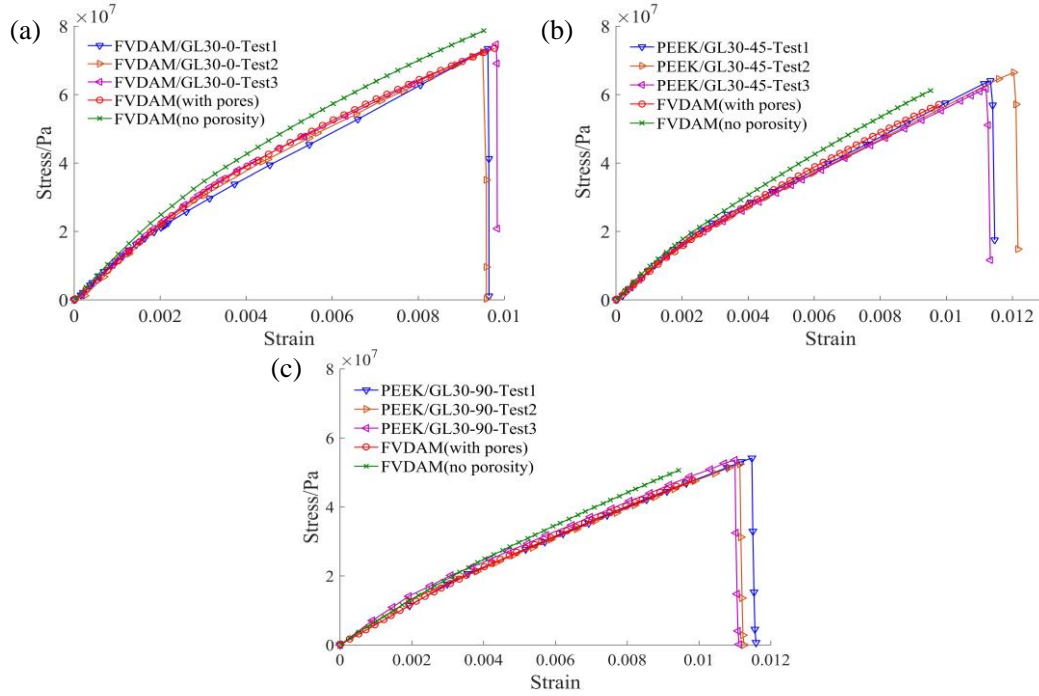


**Fig. 13.** Different off-axis angle nonlinear behaviors of fiber-reinforced composites: (a)  $0^\circ$  (b)  $45^\circ$  (c)  $90^\circ$

#### 4.4. The influence of pore ratio

Porosity represents a great influence on the mechanical properties of composites, which leads to obvious anisotropy and reduction in stiffness. In Fig. 15, the effect of 5%, 10%, 15% and 20% pore ratios on the tensile moduli  $E_{11}$  and  $E_{22}$  and Poisson's ratio  $\nu_{12}$  are evaluated using the two steps strategy, where  $E_{11}$  and  $E_{22}$  are the tensile moduli along the principle axis, i.e., in the  $0^\circ$  and  $90^\circ$  directions, respectively. In addition, the numerical results for 17.16% pore ratio, which are for the material in Table 3, are also shown in the figure. It is interesting to notice that from the figure the tensile elastic modulus and Poisson's ratio decrease nonlinearly with the increase of pore ratio. In particular, for the materials in Table 3,  $E_{11}$  and  $E_{22}$  are, respectively, 5.917GPa and 3.749GPa. The Poisson's ratio is 0.322.

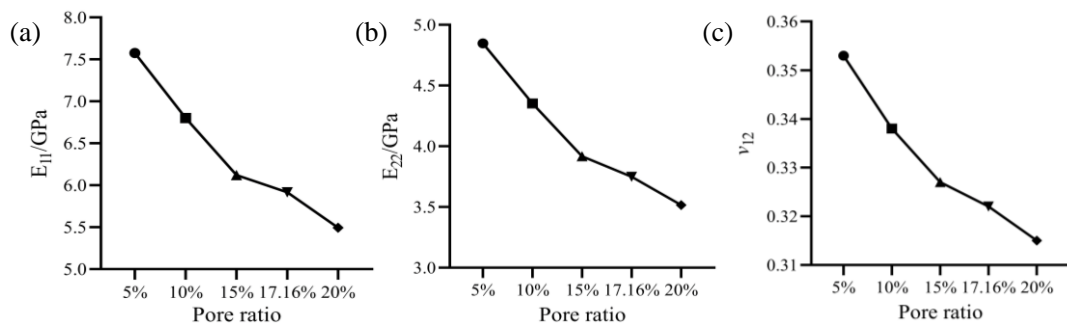


**Fig. 14.** Pore ratio influences on mechanical properties: (a) elastic modulus of  $0^\circ$  direction (b) elastic modulus of  $90^\circ$  direction (c) Poisson's ratio  $\nu_{12}$

## 5 Conclusions

In this study, a new two-step modeling strategy has been proposed to evaluate effective properties of micro-fiber reinforced composites with consideration of primary pores that may be formed during manufacturing. Micro-CT tests were conducted to obtain micro-scale geometrical morphology of the pore defects. On this basis, a micro-scale model was established and validated. The numerical

---

results showed a high consistency with the experimental data. The following conclusions are drawn from the study:

- 1) The proposed two-step modeling strategy is effectively in evaluating elastic modulus and nonlinear stress-strain relations of random micro-fiber reinforced composites with consideration of primary pores, which overcome the difficulties in predicting orthotropic mechanical properties of micro-fiber reinforced composites with pores.
- 2) Pore morphology and distribution are mainly related to matrix flow and molding pressure direction during the preparation process. Only a few pores can be found in the upper and lower surfaces of composites.
- 3) For the micro-fiber reinforced composites, the pore defects and the fibers can be considered at the same geometrical scale in numerical modelling. In addition, primary pores can be considered isotropic, which were demonstrated by the spherical analysis.

This study does not include the formation of pores in the process of manufacturing, such as the effect of flow rate and pressure on pore ratio and distribution at microscopic scale, which is currently under investigation. The additional information from further investigations will improve the accuracy of the microscopic model developed in this paper.

#### **Data availability statement**

The raw/processed data required to reproduce these findings cannot be shared at this time as the data also forms part of an ongoing study.

#### **CRedit authorship contribution statement**

**Heng Cai:** Writing-original draft, Methodology, Visualization. **Junjie Ye:** Writing-original draft, Methodology, Conceptualisation. **Jinwang Shi:** Visualization, Software. **Yiwei Wang:** Validation, Data curation; **Yang Shi:** Methodology, Visualization. **Bo Huang:** Data curation, Visualization. **Yonghe Xu:** Resources. **Mohamed Saafi:** Writing-review & editing, Supervision. **Jianqiao Ye:** Methodology, Conceptualisation, Writing-review & editing, Supervision.

#### **Declaration of Competing Interest**

The authors declare that they have no known competing financial interests or personal relationships that could have appeared to influence the work reported in this paper.

#### **Acknowledgments**

This work was supported by the National Natural Science Foundation of China, China (No. 52175112, 51675397). The National Natural Science Foundation of Shaanxi Province, China (No. 2018JZ5005). The 111 Project, China (No. B14042). China Scholarship Council (No. 202106960030). Yancheng Xinyongjia Petroleum Machinery Manufacturing CO., Ltd of China (HX01202006043). Fundamental Research Funds for the Central Universities (JB210421). Ye would like to thank the technological support from Xi'an Shiyou University for the Zeiss Xradia 510 versa and Avizo software.

#### **References**

- [1] Barari B, Simacek P, Yarlagadda S, Crane RM, Advani SG. Prediction of process-induced void formation in anisotropic Fiber-reinforced autoclave composite parts. *Int J Mater Form* 2020;13:143–58. <https://doi.org/10.1007/s12289-019-01477-4>.
- [2] Mehdikhani M, Gorbatikh L, Verpoest I, Lomov S V. Voids in fiber-reinforced polymer composites: A

- 
- review on their formation, characteristics, and effects on mechanical performance. *J Compos Mater* 2019;53:1579–669. <https://doi.org/10.1177/0021998318772152>.
- [3] Ge L, Li HM, Liu BS, Fang DN. Multi-scale elastic property prediction of 3D five-directional braided composites considering pore defects. *Compos Struct* 2020; 244: 11. <https://doi.org/10.1016/j.compstruct.2020.112287>.
- [4] Dong JW, Huo NF. A two-scale method for predicting the mechanical properties of 3D braided composites with internal defects. *Compos Struct* 2016;152:1–10. <https://doi.org/10.1016/j.compstruct.2016.05.025>.
- [5] Zhou B, Yu FG, Li H, Xin W. A Quantitative Study on the Void Defects Evolving into Damage in Wind Turbine Blade Based on Internal Energy Storage. *Appl Sci* 2020;10:13. <https://doi.org/10.3390/app10020491>.
- [6] Zhao CY, Yang B, Wang SL, Ma C, Wang SB, Bi FY. Three-Dimensional Numerical Simulation of Meso-Scale-Void Formation during the Mold-Filling Process of LCM. *Appl Compos Mater* 2019;26:1121–37. <https://doi.org/10.1007/s10443-019-09770-w>.
- [7] Wang WQ, Wu CQ, Li J, Liu ZX, Lv YP. Behavior of ultra-high performance fiber-reinforced concrete (UHPFRC) filled steel tubular members under lateral impact loading. *Int J Impact Eng* 2019;132:24. <https://doi.org/10.1016/j.ijimpeng.2019.103314>.
- [8] Xiong Q, Wang X, Jivkov AP. A 3D multi-phase meso-scale model for modelling coupling of damage and transport properties in concrete. *Cem Concr Compos* 2020;109:103545. <https://doi.org/https://doi.org/10.1016/j.cemconcomp.2020.103545>.
- [9] Ma YQ, Wang J, Zhao YT, Wei XL, Ju LY, Chen Y. A New Vacuum Pressure Infiltration CFRP Method and Preparation Experimental Study of Composite. *Polymers (Basel)* 2020;12:15. <https://doi.org/10.3390/polym12020419>.
- [10] Ye J, Chu C, Cai H, Hou X, Shi B, Tian S, et al. A multi-scale model for studying failure mechanisms of composite wind turbine blades. *Compos Struct* 2019;212:220–9. <https://doi.org/10.1016/j.compstruct.2019.01.031>.
- [11] Xu CB, Yang ZB, Tian SH, Chen XF. Lamb wave inspection for composite laminates using a combined method of sparse reconstruction and delay-and-sum. *Compos Struct* 2019;223:10. <https://doi.org/10.1016/j.compstruct.2019.110973>.
- [12] Shi PP. Singular integral equation method for 2D fracture analysis of orthotropic solids containing doubly periodic strip-like cracks on rectangular lattice arrays under longitudinal shear loading. *Appl Math Model* 2020;77:1460–73. <https://doi.org/10.1016/j.apm.2019.09.026>.
- [13] Huang T, Gong YH. A multiscale analysis for predicting the elastic properties of 3D woven composites containing void defects. *Compos Struct* 2018;185:401–10. <https://doi.org/10.1016/j.compstruct.2017.11.046>.
- [14] Mekonnen AA, Woo K. Effects of Defects on Effective Material Properties of Triaxial Braided Textile Composite. *Int J Aeronaut Sp Sci* 2020;21:657–69. <https://doi.org/10.1007/s42405-019-00244-8>.
- [15] Wei KL, Li J, Shi HB, Tang M. Numerical evaluation on the influence of void defects and interphase on the thermal expansion coefficients of three-dimensional woven carbon/carbon composites. *Compos Interfaces* 2020;27:873–92. <https://doi.org/10.1080/09276440.2019.1707586>.
- [16] Yang PP, Hu N, Guo XJ, Dong LT, Chen Y, Guo ZY. An ultra-simple universal model for the effective elastic properties of isotropic 3D closed-cell porous materials. *Compos Struct* 2020;249:10. <https://doi.org/10.1016/j.compstruct.2020.112531>.
- [17] Cao YJ, Shen WQ, Shao JF, Wang W. Numerical homogenization of elastic properties and plastic yield stress of rock-like materials with voids and inclusions at same scale. *Eur J Mech a-Solids* 2020;81:15.

- 
- <https://doi.org/10.1016/j.euromechsol.2020.103958>.
- [18] ASTM D2734-16, Standard Test Methods for Void Content of Reinforced Plastics, ASTM International, West Conshohocken, PA, 2016, [www.astm.org](http://www.astm.org).
- [19] ASTM D3171-11, Standard Test Methods for Constituent Content of Composite Materials, ASTM International, West Conshohocken, PA, 2011, [www.astm.org](http://www.astm.org).
- [20] ASTM D2584-18, Standard Test Method for Ignition Loss of Cured Reinforced Resins, ASTM International, West Conshohocken, PA, 2018, [www.astm.org](http://www.astm.org).
- [21] Hamidi YK, Aktas L, Altan MC. Three-dimensional features of void morphology in resin transfer molded composites. *Compos Sci Technol* 2005;65:1306–20. <https://doi.org/10.1016/j.compscitech.2005.01.001>.
- [22] Lin L, Chen J, Zhang X, Li X. A novel 2-D random void model and its application in ultrasonically determined void content for composite materials. *Ndt E Int* 2011;44:254–60. <https://doi.org/10.1016/j.ndteint.2010.12.003>.
- [23] Wang PD, Lei HS, Zhu XL, Chen HS, Wang CX, Fang DN. Effect of manufacturing defect on mechanical performance of plain weave carbon/epoxy composite based on 3D geometrical reconstruction. *Compos Struct* 2018;199:38–52. <https://doi.org/10.1016/j.compstruct.2018.05.066>.
- [24] Ye J, Cai H, Liu L, Zhai Z, Victor AC, Wang Y, et al. Microscale intrinsic properties of hybrid unidirectional/woven composite laminates: Part I experimental tests. *Compos Struct* 2020:113369. <https://doi.org/10.1016/j.compstruct.2020.113369>.
- [25] Cai H, Ye JJ, Wang YW, Saafi M, Huang B, Yang DM, et al. An effective micro-scale approach for determining the anisotropy of polymer composites reinforced with randomly distributed short fibers. *Compos Struct* 2020;240:11. <https://doi.org/10.1016/j.compstruct.2020.112087>.
- [26] Jin C, Zhang WX, Yang X, Liu K. Region-based adaptive asphalt mixture microstructural modeling for efficient numerical simulation. *Constr Build Mater* 2020;257:9. <https://doi.org/10.1016/j.conbuildmat.2020.119431>.
- [27] Bansal Y, Pindera MJ. Finite-volume direct averaging micromechanics of heterogeneous materials with elastic-plastic phases. *Int J Plast* 2006;22:775–825. <https://doi.org/10.1016/j.ijplas.2005.04.012>.
- [28] Bansal Y, Pindera MJ. A second look at the higher-order theory for periodic multiphase materials. *J Appl Mech Trans ASME* 2005;72:177–95. <https://doi.org/10.1115/1.1831294>.
- [29] Ye JJ, Wang YW, Li ZW, Saafi M, Jia F, Huang B, et al. Failure analysis of fiber-reinforced composites subjected to coupled thermo-mechanical loading. *Compos Struct* 2020;235:13. <https://doi.org/10.1016/j.compstruct.2019.111756>.
- [30] Yang DH, Yang ZB, Zhai Z, Chen XF. Homogenization and Localization of Ratcheting Behavior of Composite Materials and Structures with the Thermal Residual Stress Effect. *Materials (Basel)* 2019;12:20. <https://doi.org/10.3390/ma12183048>.
- [31] Ye J, Hong Y, Cai H, Wang Y, Zhai Z, Shi B. A new three-dimensional parametric FVDAM for investigating the effective elastic moduli of particle-reinforced composites with interphase. *Mech Adv Mater Struct* 2019;26:1870–80. <https://doi.org/10.1080/15376494.2018.1452321>.
- [32] Chen Q, Chen X, Zhai Z, Yang Z. A new and general formulation of three-dimensional finite-volume micromechanics for particulate reinforced composites with viscoplastic phases. *Compos Part B Eng* 2016;85:216–32. <https://doi.org/10.1016/j.compositesb.2015.09.014>.
- [33] Cavalcante MAA, Pindera M-J. Generalized FVDAM Theory for Periodic Materials Undergoing Finite Deformations-Part I: Framework. *J Appl Mech Asme* 2014;81. <https://doi.org/10.1115/1.4024406>.
- [34] Cavalcante MAA, Marques SPC. Homogenization of periodic materials with viscoelastic phases using the generalized FVDAM theory. *Comput Mater Sci* 2014;87:43–53. <https://doi.org/10.1016/j.commatsci.2014>.

01. 053.
- [35] Feng XQ, Mai YW, Qin QH. A micromechanical model for interpenetrating multiphase composites. *Comput. Mater. Sci.*, vol. 28, 2003, p. 486–93. <https://doi.org/10.1016/j.commat.2003.06.005>.
- [36] Hill R. A self-consistent mechanics of composite materials. *J Mech Phys solids*, 1965, 13(4): 213-222. [https://doi.org/10.1016/0022-5096\(65\)90010-4](https://doi.org/10.1016/0022-5096(65)90010-4)
- [37] Liu J, Zuo F, Liu C. A Trans-Scale Young' Modulus Calculation Model of ITZ Based on Void Shape Randomness and Calcium Hydroxide Enrichment. *Adv Mater Sci Eng* 2020;2020. <https://doi.org/10.1155/2020/9430875>.
- [38] Cai H, Ye J, Wang Y, Jia F, Hong Y, Tian S, et al. Matrix failures effect on damage evolution of particle reinforced composites. *Mech Adv Mater Struct* 2019;1–13. <https://doi.org/10.1080/15376494.2019.1579396>.
- [39] Bodner Sr, Partom Y. Constitutive equations for elastic-viscoplastic strain-hardening materials 1975.
- [40] Chen Q, Chen X, Zhai Z, Zhu X, Yang Z. Micromechanical Modeling of Viscoplastic Behavior of Laminated Polymer Composites With Thermal Residual Stress Effect. *J Eng Mater Technol* 2016;138. <https://doi.org/10.1115/1.4033070>.

## Appendix A

$$\begin{aligned}
 \varepsilon_{11}(x, y) &= \bar{\varepsilon}_{11} + \frac{\partial u'_1}{\partial y_1} = \bar{\varepsilon}_{11} + \bar{J}_{11} \frac{\partial u'_1}{\partial \zeta} + \bar{J}_{12} \frac{\partial u'_1}{\partial \eta} + \bar{J}_{13} \frac{\partial u'_1}{\partial \xi} \\
 \varepsilon_{22}(x, y) &= \bar{\varepsilon}_{22} + \frac{\partial u'_2}{\partial y_2} = \bar{\varepsilon}_{22} + \bar{J}_{21} \frac{\partial u'_2}{\partial \zeta} + \bar{J}_{22} \frac{\partial u'_2}{\partial \eta} + \bar{J}_{23} \frac{\partial u'_2}{\partial \xi} \\
 \varepsilon_{33}(x, y) &= \bar{\varepsilon}_{33} + \frac{\partial u'_3}{\partial y_3} = \bar{\varepsilon}_{33} + \bar{J}_{31} \frac{\partial u'_3}{\partial \zeta} + \bar{J}_{32} \frac{\partial u'_3}{\partial \eta} + \bar{J}_{33} \frac{\partial u'_3}{\partial \xi} \\
 \varepsilon_{23}(x, y) &= \bar{\varepsilon}_{23} + \frac{1}{2} \left( \frac{\partial u'_2}{\partial y_3} + \frac{\partial u'_3}{\partial y_2} \right) = \bar{\varepsilon}_{23} + \frac{1}{2} \left( \bar{J}_{31} \frac{\partial u'_2}{\partial \zeta} + \bar{J}_{32} \frac{\partial u'_2}{\partial \eta} + \bar{J}_{33} \frac{\partial u'_2}{\partial \xi} \right) + \frac{1}{2} \left( \bar{J}_{21} \frac{\partial u'_3}{\partial \zeta} + \bar{J}_{22} \frac{\partial u'_3}{\partial \eta} + \bar{J}_{23} \frac{\partial u'_3}{\partial \xi} \right) \\
 \varepsilon_{12}(x, y) &= \bar{\varepsilon}_{12} + \frac{1}{2} \left( \frac{\partial u'_1}{\partial y_2} + \frac{\partial u'_2}{\partial y_1} \right) = \bar{\varepsilon}_{12} + \frac{1}{2} \left( \bar{J}_{21} \frac{\partial u'_1}{\partial \zeta} + \bar{J}_{22} \frac{\partial u'_1}{\partial \eta} + \bar{J}_{23} \frac{\partial u'_1}{\partial \xi} \right) + \frac{1}{2} \left( \bar{J}_{11} \frac{\partial u'_2}{\partial \zeta} + \bar{J}_{12} \frac{\partial u'_2}{\partial \eta} + \bar{J}_{13} \frac{\partial u'_2}{\partial \xi} \right) \\
 \varepsilon_{13}(x, y) &= \bar{\varepsilon}_{13} + \frac{1}{2} \left( \frac{\partial u'_1}{\partial y_3} + \frac{\partial u'_3}{\partial y_1} \right) = \bar{\varepsilon}_{13} + \frac{1}{2} \left( \bar{J}_{31} \frac{\partial u'_1}{\partial \zeta} + \bar{J}_{32} \frac{\partial u'_1}{\partial \eta} + \bar{J}_{33} \frac{\partial u'_1}{\partial \xi} \right) + \frac{1}{2} \left( \bar{J}_{11} \frac{\partial u'_3}{\partial \zeta} + \bar{J}_{12} \frac{\partial u'_3}{\partial \eta} + \bar{J}_{13} \frac{\partial u'_3}{\partial \xi} \right)
 \end{aligned} \tag{A.1}$$

$$\begin{aligned}
 \sigma_{11}^{(\alpha\beta\gamma)} &= C_{11}^{(\alpha\beta\gamma)} (\bar{\varepsilon}_{11} + \bar{J}_{11}^{(\alpha\beta\gamma)} [W_{1(100)}^{(\alpha\beta\gamma)} + 3\zeta W_{1(200)}^{(\alpha\beta\gamma)}] + \bar{J}_{12}^{(\alpha\beta\gamma)} [W_{1(010)}^{(\alpha\beta\gamma)} + 3\eta W_{1(020)}^{(\alpha\beta\gamma)}] + \bar{J}_{13}^{(\alpha\beta\gamma)} [W_{1(001)}^{(\alpha\beta\gamma)} + 3\xi W_{1(002)}^{(\alpha\beta\gamma)}] - \varepsilon_{11}^{in(\alpha\beta\gamma)}) + \\
 &C_{12}^{(\alpha\beta\gamma)} (\bar{\varepsilon}_{22} + \bar{J}_{21}^{(\alpha\beta\gamma)} [W_{2(100)}^{(\alpha\beta\gamma)} + 3\zeta W_{2(200)}^{(\alpha\beta\gamma)}] + \bar{J}_{22}^{(\alpha\beta\gamma)} [W_{2(010)}^{(\alpha\beta\gamma)} + 3\eta W_{2(020)}^{(\alpha\beta\gamma)}] + \bar{J}_{23}^{(\alpha\beta\gamma)} [W_{2(001)}^{(\alpha\beta\gamma)} + 3\xi W_{2(002)}^{(\alpha\beta\gamma)}] - \varepsilon_{22}^{in(\alpha\beta\gamma)}) + \\
 &C_{13}^{(\alpha\beta\gamma)} (\bar{\varepsilon}_{33} + \bar{J}_{31}^{(\alpha\beta\gamma)} [W_{3(100)}^{(\alpha\beta\gamma)} + 3\zeta W_{3(200)}^{(\alpha\beta\gamma)}] + \bar{J}_{32}^{(\alpha\beta\gamma)} [W_{3(010)}^{(\alpha\beta\gamma)} + 3\eta W_{3(020)}^{(\alpha\beta\gamma)}] + \bar{J}_{33}^{(\alpha\beta\gamma)} [W_{3(001)}^{(\alpha\beta\gamma)} + 3\xi W_{3(002)}^{(\alpha\beta\gamma)}] - \varepsilon_{33}^{in(\alpha\beta\gamma)}) \\
 \sigma_{22}^{(\alpha\beta\gamma)} &= C_{21}^{(\alpha\beta\gamma)} (\bar{\varepsilon}_{11} + \bar{J}_{11}^{(\alpha\beta\gamma)} [W_{1(100)}^{(\alpha\beta\gamma)} + 3\zeta W_{1(200)}^{(\alpha\beta\gamma)}] + \bar{J}_{12}^{(\alpha\beta\gamma)} [W_{1(010)}^{(\alpha\beta\gamma)} + 3\eta W_{1(020)}^{(\alpha\beta\gamma)}] + \bar{J}_{13}^{(\alpha\beta\gamma)} [W_{1(001)}^{(\alpha\beta\gamma)} + 3\xi W_{1(002)}^{(\alpha\beta\gamma)}] - \varepsilon_{11}^{in(\alpha\beta\gamma)}) + \\
 &C_{22}^{(\alpha\beta\gamma)} (\bar{\varepsilon}_{22} + \bar{J}_{21}^{(\alpha\beta\gamma)} [W_{2(100)}^{(\alpha\beta\gamma)} + 3\zeta W_{2(200)}^{(\alpha\beta\gamma)}] + \bar{J}_{22}^{(\alpha\beta\gamma)} [W_{2(010)}^{(\alpha\beta\gamma)} + 3\eta W_{2(020)}^{(\alpha\beta\gamma)}] + \bar{J}_{23}^{(\alpha\beta\gamma)} [W_{2(001)}^{(\alpha\beta\gamma)} + 3\xi W_{2(002)}^{(\alpha\beta\gamma)}] - \varepsilon_{22}^{in(\alpha\beta\gamma)}) + \\
 &C_{23}^{(\alpha\beta\gamma)} (\bar{\varepsilon}_{33} + \bar{J}_{31}^{(\alpha\beta\gamma)} [W_{3(100)}^{(\alpha\beta\gamma)} + 3\zeta W_{3(200)}^{(\alpha\beta\gamma)}] + \bar{J}_{32}^{(\alpha\beta\gamma)} [W_{3(010)}^{(\alpha\beta\gamma)} + 3\eta W_{3(020)}^{(\alpha\beta\gamma)}] + \bar{J}_{33}^{(\alpha\beta\gamma)} [W_{3(001)}^{(\alpha\beta\gamma)} + 3\xi W_{3(002)}^{(\alpha\beta\gamma)}] - \varepsilon_{33}^{in(\alpha\beta\gamma)}) \\
 \sigma_{33}^{(\alpha\beta\gamma)} &= C_{31}^{(\alpha\beta\gamma)} (\bar{\varepsilon}_{11} + \bar{J}_{11}^{(\alpha\beta\gamma)} [W_{1(100)}^{(\alpha\beta\gamma)} + 3\zeta W_{1(200)}^{(\alpha\beta\gamma)}] + \bar{J}_{12}^{(\alpha\beta\gamma)} [W_{1(010)}^{(\alpha\beta\gamma)} + 3\eta W_{1(020)}^{(\alpha\beta\gamma)}] + \bar{J}_{13}^{(\alpha\beta\gamma)} [W_{1(001)}^{(\alpha\beta\gamma)} + 3\xi W_{1(002)}^{(\alpha\beta\gamma)}] - \varepsilon_{11}^{in(\alpha\beta\gamma)}) + \\
 &C_{32}^{(\alpha\beta\gamma)} (\bar{\varepsilon}_{22} + \bar{J}_{21}^{(\alpha\beta\gamma)} [W_{2(100)}^{(\alpha\beta\gamma)} + 3\zeta W_{2(200)}^{(\alpha\beta\gamma)}] + \bar{J}_{22}^{(\alpha\beta\gamma)} [W_{2(010)}^{(\alpha\beta\gamma)} + 3\eta W_{2(020)}^{(\alpha\beta\gamma)}] + \bar{J}_{23}^{(\alpha\beta\gamma)} [W_{2(001)}^{(\alpha\beta\gamma)} + 3\xi W_{2(002)}^{(\alpha\beta\gamma)}] - \varepsilon_{22}^{in(\alpha\beta\gamma)}) + \\
 &C_{33}^{(\alpha\beta\gamma)} (\bar{\varepsilon}_{33} + \bar{J}_{31}^{(\alpha\beta\gamma)} [W_{3(100)}^{(\alpha\beta\gamma)} + 3\zeta W_{3(200)}^{(\alpha\beta\gamma)}] + \bar{J}_{32}^{(\alpha\beta\gamma)} [W_{3(010)}^{(\alpha\beta\gamma)} + 3\eta W_{3(020)}^{(\alpha\beta\gamma)}] + \bar{J}_{33}^{(\alpha\beta\gamma)} [W_{3(001)}^{(\alpha\beta\gamma)} + 3\xi W_{3(002)}^{(\alpha\beta\gamma)}] - \varepsilon_{33}^{in(\alpha\beta\gamma)}) \\
 \sigma_{23}^{(\alpha\beta\gamma)} &= 2C_{44}^{(\alpha\beta\gamma)} (\bar{\varepsilon}_{23} + \frac{1}{2} \{ \bar{J}_{31}^{(\alpha\beta\gamma)} [W_{2(100)}^{(\alpha\beta\gamma)} + 3\zeta W_{2(200)}^{(\alpha\beta\gamma)}] + \bar{J}_{32}^{(\alpha\beta\gamma)} [W_{2(010)}^{(\alpha\beta\gamma)} + 3\eta W_{2(020)}^{(\alpha\beta\gamma)}] + \bar{J}_{33}^{(\alpha\beta\gamma)} [W_{2(001)}^{(\alpha\beta\gamma)} + 3\xi W_{2(002)}^{(\alpha\beta\gamma)}] + \\
 &\bar{J}_{21}^{(\alpha\beta\gamma)} [W_{3(100)}^{(\alpha\beta\gamma)} + 3\zeta W_{3(200)}^{(\alpha\beta\gamma)}] + \bar{J}_{22}^{(\alpha\beta\gamma)} [W_{3(010)}^{(\alpha\beta\gamma)} + 3\eta W_{3(020)}^{(\alpha\beta\gamma)}] + \bar{J}_{23}^{(\alpha\beta\gamma)} [W_{3(001)}^{(\alpha\beta\gamma)} + 3\xi W_{3(002)}^{(\alpha\beta\gamma)}] \} - \varepsilon_{23}^{in(\alpha\beta\gamma)}) \\
 \sigma_{13}^{(\alpha\beta\gamma)} &= 2C_{55}^{(\alpha\beta\gamma)} (\bar{\varepsilon}_{13} + \frac{1}{2} \{ \bar{J}_{31}^{(\alpha\beta\gamma)} [W_{1(100)}^{(\alpha\beta\gamma)} + 3\zeta W_{1(200)}^{(\alpha\beta\gamma)}] + \bar{J}_{32}^{(\alpha\beta\gamma)} [W_{1(010)}^{(\alpha\beta\gamma)} + 3\eta W_{1(020)}^{(\alpha\beta\gamma)}] + \bar{J}_{33}^{(\alpha\beta\gamma)} [W_{1(001)}^{(\alpha\beta\gamma)} + 3\xi W_{1(002)}^{(\alpha\beta\gamma)}] + \\
 &\bar{J}_{11}^{(\alpha\beta\gamma)} [W_{3(100)}^{(\alpha\beta\gamma)} + 3\zeta W_{3(200)}^{(\alpha\beta\gamma)}] + \bar{J}_{12}^{(\alpha\beta\gamma)} [W_{3(010)}^{(\alpha\beta\gamma)} + 3\eta W_{3(020)}^{(\alpha\beta\gamma)}] + \bar{J}_{13}^{(\alpha\beta\gamma)} [W_{3(001)}^{(\alpha\beta\gamma)} + 3\xi W_{3(002)}^{(\alpha\beta\gamma)}] \} - \varepsilon_{13}^{in(\alpha\beta\gamma)}) \\
 \sigma_{12}^{(\alpha\beta\gamma)} &= 2C_{66}^{(\alpha\beta\gamma)} (\bar{\varepsilon}_{12} + \frac{1}{2} \{ \bar{J}_{21}^{(\alpha\beta\gamma)} [W_{1(100)}^{(\alpha\beta\gamma)} + 3\zeta W_{1(200)}^{(\alpha\beta\gamma)}] + \bar{J}_{22}^{(\alpha\beta\gamma)} [W_{1(010)}^{(\alpha\beta\gamma)} + 3\eta W_{1(020)}^{(\alpha\beta\gamma)}] + \bar{J}_{23}^{(\alpha\beta\gamma)} [W_{1(001)}^{(\alpha\beta\gamma)} + 3\xi W_{1(002)}^{(\alpha\beta\gamma)}] + \\
 &\bar{J}_{11}^{(\alpha\beta\gamma)} [W_{2(100)}^{(\alpha\beta\gamma)} + 3\zeta W_{2(200)}^{(\alpha\beta\gamma)}] + \bar{J}_{12}^{(\alpha\beta\gamma)} [W_{2(010)}^{(\alpha\beta\gamma)} + 3\eta W_{2(020)}^{(\alpha\beta\gamma)}] + \bar{J}_{13}^{(\alpha\beta\gamma)} [W_{2(001)}^{(\alpha\beta\gamma)} + 3\xi W_{2(002)}^{(\alpha\beta\gamma)}] \} - \varepsilon_{12}^{in(\alpha\beta\gamma)})
 \end{aligned} \tag{A.2}$$







$$\begin{bmatrix} \bar{l}_1^{-1} \\ \bar{l}_2^{-1} \\ \bar{l}_3^{-1} \\ \bar{l}_1^{-2} \\ \bar{l}_2^{-2} \\ \bar{l}_3^{-2} \\ \bar{l}_1^{-3} \\ \bar{l}_2^{-3} \\ \bar{l}_3^{-3} \\ \bar{l}_1^{-4} \\ \bar{l}_2^{-4} \\ \bar{l}_3^{-4} \\ \bar{l}_1^{-5} \\ \bar{l}_2^{-5} \\ \bar{l}_3^{-5} \\ \bar{l}_1^{-6} \\ \bar{l}_2^{-6} \\ \bar{l}_3^{-6} \end{bmatrix}^{(\alpha\beta\gamma)} = \begin{bmatrix} K_{aa} & K_{ab} & K_{ac} & K_{ad} & K_{ae} & K_{af} & K_{ag} & K_{ah} & K_{ai} & K_{aj} & K_{ak} & K_{al} & K_{am} & K_{an} & K_{ao} & K_{ap} & K_{aq} & K_{ar} \\ K_{ba} & K_{bb} & K_{bc} & K_{bd} & K_{be} & K_{bf} & K_{bg} & K_{bh} & K_{bi} & K_{bj} & K_{bk} & K_{bl} & K_{bm} & K_{bn} & K_{bo} & K_{bp} & K_{bq} & K_{br} \\ K_{ca} & K_{cb} & K_{cc} & K_{cd} & K_{ce} & K_{cf} & K_{cg} & K_{ch} & K_{ci} & K_{cj} & K_{ck} & K_{cl} & K_{cm} & K_{cn} & K_{co} & K_{cp} & K_{cq} & K_{cr} \\ K_{da} & K_{db} & K_{dc} & K_{dd} & K_{de} & K_{df} & K_{dg} & K_{dh} & K_{di} & K_{dj} & K_{dk} & K_{dl} & K_{dm} & K_{dn} & K_{do} & K_{dp} & K_{dq} & K_{dr} \\ K_{ea} & K_{eb} & K_{ec} & K_{ed} & K_{ee} & K_{ef} & K_{eg} & K_{eh} & K_{ei} & K_{ej} & K_{ek} & K_{el} & K_{em} & K_{en} & K_{eo} & K_{ep} & K_{eq} & K_{er} \\ K_{fa} & K_{fb} & K_{fc} & K_{fd} & K_{fe} & K_{ff} & K_{fg} & K_{fh} & K_{fi} & K_{fj} & K_{fk} & K_{fl} & K_{fm} & K_{fn} & K_{fo} & K_{fp} & K_{fq} & K_{fr} \\ K_{ga} & K_{gb} & K_{gc} & K_{gd} & K_{ge} & K_{gf} & K_{gg} & K_{gh} & K_{gi} & K_{gj} & K_{gk} & K_{gl} & K_{gm} & K_{gn} & K_{go} & K_{gp} & K_{gq} & K_{gr} \\ K_{ha} & K_{hb} & K_{hc} & K_{hd} & K_{he} & K_{hf} & K_{hg} & K_{hh} & K_{hi} & K_{hj} & K_{hk} & K_{hl} & K_{hm} & K_{hn} & K_{ho} & K_{hp} & K_{hq} & K_{hr} \\ K_{ia} & K_{ib} & K_{ic} & K_{id} & K_{ie} & K_{if} & K_{ig} & K_{ih} & K_{ii} & K_{ij} & K_{ik} & K_{il} & K_{im} & K_{in} & K_{io} & K_{ip} & K_{iq} & K_{ir} \\ K_{ja} & K_{jb} & K_{jc} & K_{jd} & K_{je} & K_{jf} & K_{jg} & K_{jh} & K_{ji} & K_{jj} & K_{jk} & K_{jl} & K_{jm} & K_{jn} & K_{jo} & K_{jp} & K_{jq} & K_{jr} \\ K_{ka} & K_{kb} & K_{kc} & K_{kd} & K_{ke} & K_{kf} & K_{kg} & K_{kh} & K_{ki} & K_{kj} & K_{kk} & K_{kl} & K_{km} & K_{kn} & K_{ko} & K_{kp} & K_{kq} & K_{kr} \\ K_{la} & K_{lb} & K_{lc} & K_{ld} & K_{le} & K_{lf} & K_{lg} & K_{lh} & K_{li} & K_{lj} & K_{lk} & K_{ll} & K_{lm} & K_{ln} & K_{lo} & K_{lp} & K_{lq} & K_{lr} \\ K_{ma} & K_{mb} & K_{mc} & K_{md} & K_{me} & K_{mf} & K_{mg} & K_{mh} & K_{mi} & K_{mj} & K_{mk} & K_{ml} & K_{mm} & K_{mn} & K_{mo} & K_{mp} & K_{mq} & K_{mr} \\ K_{na} & K_{nb} & K_{nc} & K_{nd} & K_{ne} & K_{nf} & K_{ng} & K_{nh} & K_{ni} & K_{nj} & K_{nk} & K_{nl} & K_{nm} & K_{nn} & K_{no} & K_{np} & K_{nq} & K_{nr} \\ K_{oa} & K_{ob} & K_{oc} & K_{od} & K_{oe} & K_{of} & K_{og} & K_{oh} & K_{oi} & K_{oj} & K_{ok} & K_{ol} & K_{om} & K_{on} & K_{oo} & K_{op} & K_{oq} & K_{or} \\ K_{pa} & K_{pb} & K_{pc} & K_{pd} & K_{pe} & K_{pf} & K_{pg} & K_{ph} & K_{pi} & K_{pj} & K_{pk} & K_{pl} & K_{pm} & K_{pn} & K_{po} & K_{pp} & K_{pq} & K_{pr} \\ K_{qa} & K_{qb} & K_{qc} & K_{qd} & K_{qe} & K_{qf} & K_{qg} & K_{qh} & K_{qi} & K_{qj} & K_{qk} & K_{ql} & K_{qm} & K_{qn} & K_{qo} & K_{qp} & K_{qq} & K_{qr} \\ K_{ra} & K_{rb} & K_{rc} & K_{rd} & K_{re} & K_{rf} & K_{rg} & K_{rh} & K_{ri} & K_{rj} & K_{rk} & K_{rl} & K_{rm} & K_{rn} & K_{ro} & K_{rp} & K_{rq} & K_{rr} \end{bmatrix}^{(\alpha\beta\gamma)} \begin{bmatrix} \bar{u}_1^{-1} \\ \bar{u}_2^{-1} \\ \bar{u}_3^{-1} \\ \bar{u}_1^{-2} \\ \bar{u}_2^{-2} \\ \bar{u}_3^{-2} \\ \bar{u}_1^{-3} \\ \bar{u}_2^{-3} \\ \bar{u}_3^{-3} \\ \bar{u}_1^{-4} \\ \bar{u}_2^{-4} \\ \bar{u}_3^{-4} \\ \bar{u}_1^{-5} \\ \bar{u}_2^{-5} \\ \bar{u}_3^{-5} \\ \bar{u}_1^{-6} \\ \bar{u}_2^{-6} \\ \bar{u}_3^{-6} \end{bmatrix}^{(\alpha\beta\gamma)}$$

$$+ \begin{bmatrix} n_1^1 & 0 & 0 & 0 & n_3^1 & n_2^1 \\ 0 & n_2^1 & 0 & n_3^1 & 0 & n_1^1 \\ 0 & 0 & n_3^1 & n_2^1 & n_1^1 & 0 \\ n_1^2 & 0 & 0 & 0 & n_3^2 & n_2^2 \\ 0 & n_2^2 & 0 & n_3^2 & 0 & n_1^2 \\ 0 & 0 & n_3^2 & n_2^2 & n_1^2 & 0 \\ n_1^3 & 0 & 0 & 0 & n_3^3 & n_2^3 \\ 0 & n_2^3 & 0 & n_3^3 & 0 & n_1^3 \\ 0 & 0 & n_3^3 & n_2^3 & n_1^3 & 0 \\ n_1^4 & 0 & 0 & 0 & n_3^4 & n_2^4 \\ 0 & n_2^4 & 0 & n_3^4 & 0 & n_1^4 \\ 0 & 0 & n_3^4 & n_2^4 & n_1^4 & 0 \\ n_1^5 & 0 & 0 & 0 & n_3^5 & n_2^5 \\ 0 & n_2^5 & 0 & n_3^5 & 0 & n_1^5 \\ 0 & 0 & n_3^5 & n_2^5 & n_1^5 & 0 \\ n_1^6 & 0 & 0 & 0 & n_3^6 & n_2^6 \\ 0 & n_2^6 & 0 & n_3^6 & 0 & n_1^6 \\ 0 & 0 & n_3^6 & n_2^6 & n_1^6 & 0 \end{bmatrix}^{(\alpha\beta\gamma)}$$

$$\begin{bmatrix} C_{11} & C_{12} & C_{13} & 0 & 0 & 0 \\ C_{21} & C_{22} & C_{23} & 0 & 0 & 0 \\ C_{31} & C_{32} & C_{33} & 0 & 0 & 0 \\ 0 & 0 & 0 & C_{44} & 0 & 0 \\ 0 & 0 & 0 & 0 & C_{55} & 0 \\ 0 & 0 & 0 & 0 & 0 & C_{66} \end{bmatrix}^{(\alpha\beta\gamma)} \begin{bmatrix} \bar{\varepsilon}_{11} - \varepsilon_{11}^{in(\alpha\beta\gamma)} \\ \bar{\varepsilon}_{22} - \varepsilon_{22}^{in(\alpha\beta\gamma)} \\ \bar{\varepsilon}_{33} - \varepsilon_{33}^{in(\alpha\beta\gamma)} \\ 2\bar{\varepsilon}_{23} - 2\varepsilon_{23}^{in(\alpha\beta\gamma)} \\ 2\bar{\varepsilon}_{13} - 2\varepsilon_{13}^{in(\alpha\beta\gamma)} \\ 2\bar{\varepsilon}_{12} - 2\varepsilon_{12}^{in(\alpha\beta\gamma)} \end{bmatrix}$$

(A.11)





